Tribology International 57 (2013) 54–66

Contents lists available at SciVerse ScienceDirect

Tribology International

journal homepage: www.elsevier.com/locate/triboint

Conservative one-dimensional finite volume discretization of a new cavitation model for piston–ring lubrication

Roberto F. Ausas [a,*], Mohammed Jai [b], Ionel S. Ciuperca [c], Gustavo C. Buscaglia [a]

[a] Instituto de Ciências Matemáticas e de Computação, Universidade de São Paulo, Av. do Trabalhador São-carlense 400, 13560-970 São Carlos, SP, Brazil
[b] NRS-UMR 5208, Mathématiques, INSA de LYON, Bat Leonard de Vinci, F-69621 Villeurbanne, France
[c] CNRS-UMR 5208, Université Lyon 1, MAPLY, Bat. 101, 69622 Villeurbanne cedex, France

ARTICLE INFO

Article history:
Received 28 February 2012
Received in revised form
2 July 2012
Accepted 4 July 2012
Available online 17 July 2012

Keywords:
Hydrodynamic lubrication
Cavitation
Elrod–Adams model
Piston–rings

ABSTRACT

This paper presents a conservative numerical implementation of a new cavitation model that is well suited for lubrication problems with cavitated regions in which the fluid film is attached to just one of the participating surfaces, as happens for instance in piston–ring assemblies. This new model was recently proposed by Buscaglia et al. (2011) and is the first successful attempt at modifying the Elrod–Adams model considering a physically realistic value for the lubricant transport velocity in the incomplete-film region in those cases. In this work we show first the reasons for previous attempts to have failed, which come from a loss of uniqueness of the associated exact mathematical problem. Then, the new model is briefly recalled and a one dimensional numerical implementation by means of a finite volume scheme is presented together with several test-case results.

1. Motivation

The main function of piston–rings is to seal the space between the piston and the liner, acting as slider bearings subjected to alternating motion. These systems have been thoroughly studied before (see for instance [1–5]). Among the many reciprocating components present in internal combustion engines, piston–rings/liner contacts are responsible of an important part of the total power loss due to friction; therefore, it is of great concern whether the friction can be diminished, for instance, by texturing the surfaces with microtextures, that are now a days produced with well defined sizes and shapes using different techniques available in the industry. At the theoretical level, the effect of textures on the performance of lubricated devices is not fully understood. Though some experimental data are available (see, e.g., [6–10]) suggesting that a friction reduction can be achieved, at least in the mixed lubrication regime, numerical studies are more difficult to find (e.g. [11–13]).

The key issue in the simulation of these lubricated devices is the correct treatment of cavitation phenomena by means of incorporating appropriate mass-conserving conditions at the *unknown* cavitation boundaries. By simple inspection of the Reynolds equation, it can be noticed that the phenomenon of cavitation may take place: due to insufficient feeding, due to a positive squeeze (i.e., a transient variation of the gap between the lubricated surfaces) or as a result of a divergent film geometry and consequently at microtextures (microcavitation).

Two models are predominantly used in hydrodynamic lubrication: the Reynolds model and the Elrod–Adams model [14]. The former, easier to implement numerically, though being non-conservative, gives reasonable predictions in many cases and is thus still used in engineering practice. In the Elrod–Adams model, the JFO conditions proposed by Jacobson and Floberg [15] and Olsson [16] are applied at the cavitation boundary to enforce mass conservation. However, due to the highly non-linear nature of the problem, numerical implementations of this model are more prone to numerical instabilities. Implementations of conservative algorithms can be found for instance in [17–19]. The importance of using a conservative model has been shown by means of several numerical examples in [20,21] for problems including transient effects and/or microtextures.

Piston–ring/liner systems need special consideration, however. In the cavitated or non-pressurized region the amount of available oil is, logically, insufficient to fill the entire separation between the surfaces. For the particular case of the piston–ring/liner pair, the lubricant film remains essentially adhered to just one of the lubricated surfaces (the liner), at least far away from rupture boundaries. This is a fundamental difference with respect to other reciprocating components such as journal or thrust

* Corresponding author.
E-mail addresses: rfausas@gmail.com (R.F. Ausas), mohammed.jai@insa-lyon.fr (M. Jai), ciuperca@maply.univ-lyon1.fr (I.S. Ciuperca), gustavo.buscaglia@icmc.usp.br (G.C. Buscaglia).

0301-679X/$ - see front matter © 2012 Elsevier Ltd. All rights reserved.
http://dx.doi.org/10.1016/j.triboint.2012.07.003

bearings in which the available oil cannot be thought as attached to one specific surface of the two. This is related to the concept of streamers (see [22,23]). The mathematical and numerical modeling of piston–ring/liner systems becomes thus a challenge, since the already mentioned mathematical models do not account for this fact. Mathematically speaking, the Elrod–Adams model yields a lubricant transport velocity in the cavitated (non-pressurized) region that is half of the physically realistic value in the case of piston–rings. Now, we aim to illustrate this situation.

For this purpose, the two-phase Navier–Stokes (N–S) equations are solved and the results are compared to the Elrod–Adams (E–A) model as done in [24]. A two-dimensional implementation of an interface capturing technique is used to track the material surface separating the lubricant fluid phase from the gas phase and the N–S equations are solved on each phase. The numerical formulation adopted here is the one presented in [25], but, with surface tension effects neglected.

We consider one single ring of parabolic shape (the fix upper surface) and a flat liner (the lower surface) moving from left to right relative to the ring with a constant sliding velocity of 10 m/s as seen in Fig. 1. A viscosity equal to 2×10^{-2} Pa s is used for the lubricant phase and 2×10^{-5} Pa s for the gas phase. Densities are equal to 900 kg/m^3 and 1 kg/m^3. The minimum and maximum separations between surfaces are 6.5 μm and 50 μm, respectively (for additional details refer to [24]). As shown in the figure, at the initial time the fluid film is flat and in contact with the ring just in the central region (thin dashed line in pink color). The film profile evolves from this initial condition and at a later time ($\sim$60 μs) the result is the one drawn with thick continuous line, in blue color for the two-phase N–S formulation and in red color for the Elrod–Adams formulation. The differences are quite remarkable. First, the reformation discontinuity of the film profile (to the left of the minimum thickness point) travels faster to the left in the N–S solution than in the E–A one. Second, and perhaps more important, at the rupture point P (to the right of the minimum thickness point), the N–S formulation predicts a discontinuity of the profile (rupture meniscus) that is absent in the E–A model. Therefore, the size of the pressurized region, and thus the lift and friction forces, will significantly differ from one model to the other. Specifically, the lift force corresponding to the N–S solution is 358.5 N/m and that corresponding to the E–A solution is 247.7 N/m.

Previous attempts at modifying the E–A model so as to improve the agreement with Navier–Stokes results have lead to ill-posed mathematical problems (see [24,26]). A new lubrication model that successfully addressed the problem has been introduced in [27]. The purpose of this paper is to propose a conservative finite volume method for the new model, and to show some of the model's results in non-trivial situations.

By way of outline, after this introduction, the mathematical model and the governing equations for the new model are briefly recalled. After that, the numerical procedure for the one-dimensional case is presented. We restrict ourselves to the case of constant sliding velocity for the sake of simplicity. In the Results section, several problems are presented: first, a case with known exact solution. It consists of a single ring on a smooth liner and is solved to show convergence of the numerical predictions as a function of the grid size. Second, the case of a moving texture on the liner with two rings is simulated. This case is important because the ring upstream can influence the one downstream. Comparisons to the Elrod–Adams model are presented for this case. Finally, an example with a transient applied load is presented, in which the dynamical equilibrium equations governing the evolution of the ring are simultaneously solved with the new model equations.

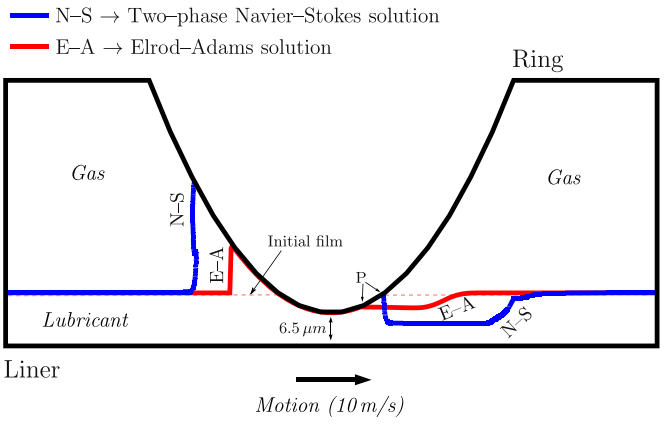

Fig. 1. Comparison of the two-phase Navier–Stokes solution with the Elrod–Adams solution for a single parabolic ring. (For interpretation of the references to color in this figure caption, the reader is referred to the web version of this article.)

2. Mathematical model

We consider a domain $\Omega\subset\mathbb{R}^d$ (d=1 or 2) divided through a cavitation boundary Σ into two regions: the pressurized region (or full-film region) and the cavitated region (or incomplete-film region) as shown in Fig. 2. In piston–ring/liner systems, the velocity profile in the incomplete-film region is planar as a consequence of having the lubricant film attached to just one of the participating surfaces. In the pressurized region, on the other hand, the velocity profile is linear or parabolic (i.e., a Poiseuille/Couette flow) depending on the pressure gradient.

The two subdomains in which Ω is divided are labeled as Ω_+ and Ω_0 and defined as follows:

$$\Omega_+(t)=\{\vec{x}\in\Omega, p(\vec{x},t)>0\} \tag{1}$$

$$\Omega_0(t)=\{\vec{x}\in\Omega, p(\vec{x},t)=0\} \tag{2}$$

where p is the pressure field. The two regions are coupled through the conservation conditions (sometimes named as the Rankine–Hugoniot conditions) at the cavitation boundary, whose position

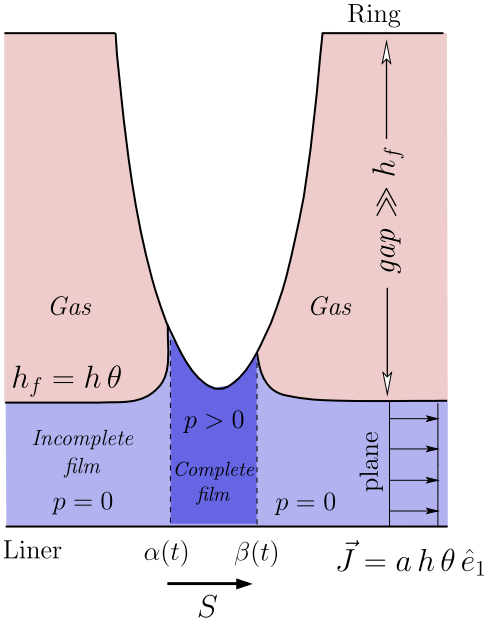

Fig. 2. Problem setting of the piston–ring/liner system.

is to be determined. The problem is governed by an elliptic equation for the pressure field in the complete-film region and by a hyperbolic equation for a saturation field $\theta(\vec{x},t)$ which represents the fraction of the total gap occupied by oil, in the cavitated region, i.e. the lubricant film thickness is equal to $h(\vec{x},t)\theta(\vec{x},t)$. The problem (in non-dimensional form) reads:

"Find $(p(\vec{x},t),\theta(\vec{x},t))$ such that for the full-film region $\Omega_+(t)$, the saturation field $\theta(\vec{x},t)=1$ and the pressure field satisfies

$$\partial_t h = \nabla\cdot(h^3\nabla p) - \frac{S}{2}\hat{e}_1\cdot\nabla h \tag{3}$$

while for the incomplete-film region $\Omega_0(t)$, the pressure field $p(\vec{x},t)=0$ and the saturation field satisfies

$$\partial_t(h\theta) + aS\hat{e}_1\cdot\nabla(h\theta) = 0 \tag{4}$$

where the parameter a is to be defined".

The key issue is the treatment of the rupture boundary, at which some of the fluid detaches from the wall because otherwise the pressure would become negative. It is not clear whether, immediately after the rupture boundary, the fluid remains attached to the upper or lower surfaces. However, it is clear that further away from the rupture boundary, the fluid remains attached to the lower wall and travels at velocity S (see Fig. 2 where the gas–gap is indicated as being much bigger than the film thickness h_f). For the well-known Elrod–Adams model, the parameter a affecting the transport velocity is $a=1/2$ which, for the case of piston rings, needs to be modified. Otherwise, the film profile downstream of the first rupture point, which "feeds" the second ring, would be incorrectly predicted.

The model proposed in [27] is an attempt to fix by allowing the parameter a to take values in [1/2,1] while maintaining the well posedness of the mathematical problem. For the cases studied in this work, we make the particular choice $a=1$. More appropriate choices for this parameter and/or additional conditions at the rupture point, where the physics is unclear, should be made on a physical basis, from experiments or using other simulation strategies and are out of the scope of this paper.

Now, the condition to be satisfied at the cavitation boundary Σ is the conservation of mass

$$(\vec{J}^{+} - \vec{J}^{-})\cdot\hat{n} = (h^+\theta^+ - h^-\theta^-)\vec{V}_\Sigma\cdot\hat{n} \tag{5}$$

where $\hat{n}$ is the normal to $\Sigma(t)$ pointing outwards from $\Omega_+(t)$ and $\vec{V}_\Sigma$ is the (unknown) velocity of Σ. The flux vector $\vec{J}$ for the full-film region is given by

$$\vec{J} = -h^3\nabla p + \frac{S}{2}\hat{e}_1 h \tag{6}$$

while for the incomplete-film region is given by

$$\vec{J} = aS\hat{e}_1 h\theta \tag{7}$$

and the supraindexes "$+$" and "$-$" refer, respectively, to the right and left sided limits of $\vec{J}$ at Σ. Next we describe the new model in the one-dimensional case. For a thorough description and mathematical analysis of the new model see [27].

2.1. The new model in the one-dimensional case

We consider a one-dimensional setting. The complete formulation of the new model and its discretization in the two-dimensional case are the subject of ongoing work.

In the one-dimensional case the cavitation boundary is represented by a set of points in the computational domain $\Omega=[x_\ell,x_r]$. For the sake of simplicity in the exposition we consider the velocity $S>0$ with just one ring and thus a unique central pressurized region with boundary points denoted by $x=\alpha(t)$ and $x=\beta(t)$ (see Fig. 2). The extension to consider a velocity S of arbitrary sign and multiple rings, each one with a pressurized region and corresponding boundaries, can be easily obtained. In fact, in the results section we present numerical examples with two rings.

We describe now the different parts involved in the resolution of the new model:

○ *Initial condition*:

We consider an initial condition given by $\alpha_0=\alpha(t=0)$ and $\beta_0=\beta(t=0)$, the left and right boundaries of the pressurized region, together with the saturation field $\theta_0(x)=\theta(x,t=0)$ given for $x<\alpha_0$ and $x>\beta_0$ (see Fig. 2).

○ *Solution in the pressurized region* Ω_+:

At each time t, it is assumed that the solution of the Reynolds equation

$$\partial_x(h^3\partial_x p) = \left(\frac{S}{2}\partial_x h + \partial_t h\right) \quad \text{with } p(\alpha(t),t)=p(\beta(t),t)=0 \tag{8}$$

yields a non-negative pressure $p(x,t)$ for all $x\in(\alpha(t),\beta(t))$.

○ *Computation of front velocities*:

In order to obtain the velocities of the boundary fronts $\alpha'(t)$ and $\beta'(t)$, we apply the mass conservation given by (5) at $x=\alpha$ and $x=\beta$, using the fluxes defined by Eqs. (6) and (7), yielding

$$\alpha'(t) = \frac{-h^3(\alpha)\partial_x p(\alpha^+,t) + \frac{S}{2}h(\alpha)[1-2a\theta(\alpha^-,t)]}{h(\alpha)[1-\theta(\alpha^-,t)]} \tag{9}$$

$$\beta'(t) = \frac{-h^3(\beta)\partial_x p(\beta^-,t) + \frac{S}{2}h(\beta)[1-2a\theta(\beta^+,t)]}{h(\beta)[1-\theta(\beta^+,t)]} \tag{10}$$

Remark 1. In the steady state, $\alpha'(t)=\beta'(t)=0$. In this case (with $S>0$), the point $x=\alpha$ is termed a reformation front, since a transition from a cavitated to a pressurized region occurs, while the point $x=\beta$ is termed a rupture front, since a transition from a pressurized to a cavitated region occurs. In the transient case (i.e., when the fronts are moving), the definition is the same, provided that both $\alpha'(t)$ and $\beta'(t)$ are smaller than S.

○ *Solution in the cavitated region* Ω_0:

The equation for $\theta(x,t)$ in the cavitated region reads

$$\partial_t(\theta h) + aS\partial_x(\theta h) = 0 \tag{11}$$

for which boundary conditions are needed at the left boundary $\theta(x_\ell,t)=\theta_{\text{in}}(t)$ and at $\beta(t)$ whenever $\beta'(t)<S$ (which is in general the case).

Remember that the Elrod–Adams model and the new model being studied here differ in the treatment of the rupture boundary. For piston rings, the *physically wrong* (since $a=1/2$) Elrod–Adams model leads to a *well-posed* mathematical problem. In particular, the saturation field and the pressure gradient at $\beta(t)$ are uniquely defined, i.e.,

$$\partial_x p(\beta^-(t),t)=0 \quad \text{and} \quad \theta(\beta^+(t),t)=1 \tag{12}$$

The model of [27] aims at allowing a *physically correct* value of a (strictly greater than 1/2, in general). For such a choice of a to lead to a well-posed problem; however, an additional condition at the rupture boundaries is needed as we shall see.

Lack of uniqueness: Remember that $p\geq 0$ on Ω_+, from which it is easily seen that $\partial_x p(\beta^-(t),t)$ must be negative. Now, taking this into account and using Eq. (10), one gets

$$\theta(\beta^+(t),t) \geq F(\beta'(t)) = \frac{\frac{S}{2}-\beta'(t)}{aS-\beta'(t)} \tag{13}$$

where the function F is plotted in Fig. 3 (the continuous red line). If $a=1/2$, this condition reduces to $\theta(\beta^+(t),t)=1$ (Elrod–Adams model).

Now, if $a > 1/2$ then $\theta(\beta^+(t),t)$ is not fully determined, since, from condition (13) it can only be said that

$$\max\{0,F(\beta'(t)\} \le \theta(\beta^+(t),t) \le 1 \tag{14}$$

i.e., for any given $\beta'(t)$, $\theta(\beta^+(t),t)$ can take any value in the interval given by (14), which is represented by the green shaded region of Fig. 3. Each of these values leads to a different solution of the problem. This explains the lack of uniqueness of the model so far when $a \neq 1/2$ and the need for an additional condition in order to have a unique solution.

Recovering uniqueness: To recover uniqueness, among the multiple values possible for $\theta(\beta^+(t),t)$, we adopt a specific choice that leads to a well–posed problem, which is

$$\theta(\beta^+(t),t) = G(\beta'(t)) = \begin{cases} \dfrac{\frac{S}{2}-\beta'(t)}{aS-\beta'(t)} & \text{if } \beta'(t) \le 0 \\ \dfrac{1}{2a} & \text{if } \beta'(t) > 0 \end{cases} \tag{15}$$

(the dashed blue line in Fig. 3). This choice is convenient for numerical implementations, since it avoids the more violent behavior of F for values of β' near $S/2$.

Remark 2. By direct inspection, it can be seen that the use of Eq. (10) with this choice actually leads to a zero pressure gradient and therefore, no equation from which to obtain the velocity β' when $\beta' < 0$. This can introduce some difficulties in the numerical implementation of such model at the rupture point as explained in the next section.

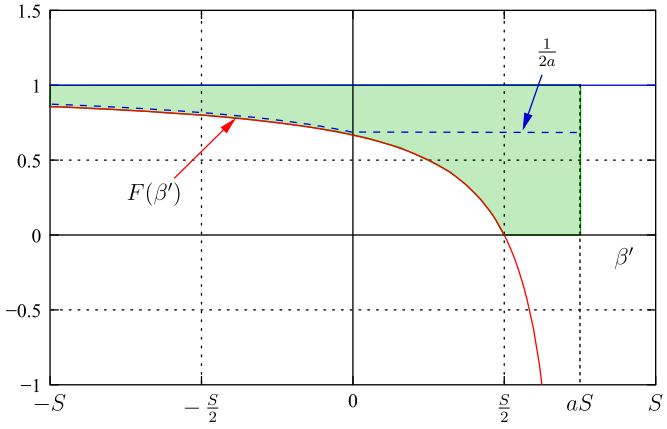

Fig. 3. Plot of the function $F(\beta')$ given in Eq. (13). (For interpretation of the references to color in this figure caption, the reader is referred to the web version of this article.)

3. Numerical method

The numerical procedure is an explicit algorithm similar to that presented in [13], though generalized to deal with more complex boundary conditions at the cavitation fronts.

From now on, we assume the value $a=1$ for the sake of simplicity. Let us also consider a time step Δt and a computational domain $[x_\ell,x_r]$ divided into cells of uniform size Δx, such that

$$t^n = n\Delta t, \quad X_i = x_\ell + i\Delta x \tag{16}$$

The time level of a discretized variable is shown as a superscript and the nodal value as a subindex. For the cavitation fronts, α^n and β^n denote the discrete values of $\alpha(t^n)$ and $\beta(t^n)$ respectively, not coincident with the grid nodes at positions X_i. At time level n, the computational domain is divided into the set of cavitated-node indices C^n ($X_i < \alpha^n$ or $X_i > \beta^n$) and the set of pressurized-node indices P^n ($\alpha^n < X_i < \beta^n$). In Fig. 4 we illustrate the finite volume discretization used for a particular case with $\alpha' < 0$ and $\beta' < 0$. We have to distinguish between the "standard" cells, defined as the intervals $[X_{i-(1/2)},X_{i+(1/2)}]$ and the two cells having α or β as cell faces, that, for the situation drawn in Fig. 4 are defined at time level $n+1$ as $[\alpha^{n+1},X_{i_\alpha+(3/2)}]$ and $[X_{i_\beta-(3/2)},\beta^{n+1}]$. We assume that always along the calculation there are several cells between the cavitation boundaries. Now, for given $\{\theta_i^n\}_{i\in C^n}$, the numerical procedure to find the new pressure and saturation field and the new position of the cavitation boundaries consists of steps 1–3 below.

1. *Numerically solve Reynolds equation for p^n*: A finite volume solver for $\{p_i^n\}_{i\in P^n}$ is used to solve Eq. (8), where P^n is the set of pressurized-node indices. The conditions $p^n(\alpha^n) = p^n(\beta^n) = 0$ are imposed placing two virtual nodes at the positions α^n and β^n. The pressure at each finite volume is found by means of an iterative procedure similar to the one described in [20]. In the kth iteration of the iterative procedure, $\{p_i^{n,k}\}_{i\in P^n}$ is found according to

$$p_i^{n,k} = \left[(h_r^n)^3\, p_{i+1}^{n,k-1} + (h_\ell^n)^3 p_{i-1}^{n,k-1} - \gamma \frac{(\Delta x)^2}{\Delta t}(h_i^{n+1} - h_i^n) - \frac{S}{2}(h_r^n - h_\ell^n)\Delta x \right] \Big/ \left[\frac{(h_r^n)^3}{\gamma_r} + \frac{(h_\ell^n)^3}{\gamma_\ell} \right] \tag{17}$$

where
   - $h_\ell^n = h_{i-\frac{1}{2}}^n$, $h_r^n = h_{i+\frac{1}{2}}^n$ and $\gamma_r = \gamma_\ell = \gamma = 1$, for the standard cells (not having α^n or β^n as left or right faces);

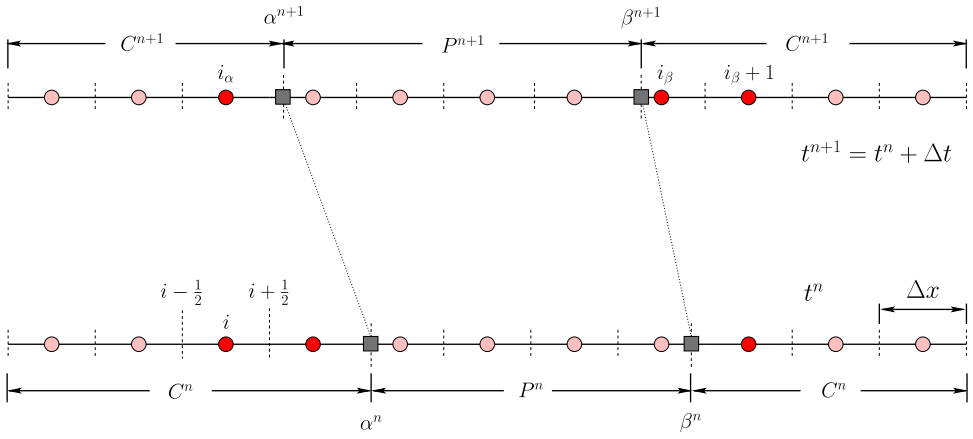

Fig. 4. Scheme of the finite volume discretization for the one-dimensional computational domain. (For interpretation of the references to color in this figure caption, the reader is referred to the web version of this article.)

- $p_{i-1}^{n,k-1}=0$, $\gamma=(X_{i+\frac{1}{2}}-\alpha^n)/\Delta x$, $\gamma_\ell=\gamma-\frac{1}{2}$, $\gamma_r=1$, $h_\ell^n=h(\alpha^n)$, $h_r^n=h_{i+\frac{1}{2}}^n$, for the cell having α^n as left face;
- $p_{i+1}^{n,k-1}=0$, $\gamma=(\beta^n-X_{i-\frac{1}{2}})/\Delta x$, $\gamma_\ell=1$, $\gamma_r=\gamma-\frac{1}{2}$, $h_\ell^n=h_{i-\frac{1}{2}}^n$, $h_r^n=h(\beta^n)$, for the cell having β^n as right face.

Iterations are done until reaching convergence of the euclidean norm of the difference between two consecutive iterations. In the numerical experiments presented a numerical tolerance of 10^{-10} is considered.

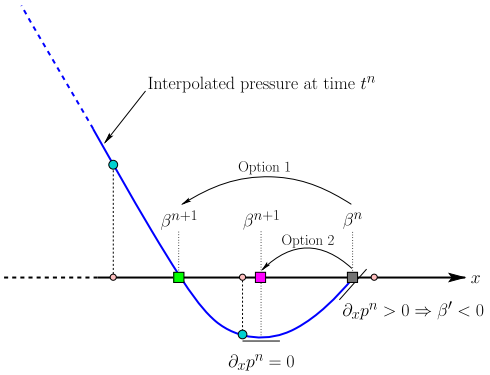

Fig. 5. Two options considered to find β^{n+1} in the case of a negative front velocity β'.

Remark 3. This computation may result in a negative pressure region to the left of β^n, which has to be considered in the next step.

2. *Compute* α^{n+1} *and* β^{n+1}: Here we use explicit updating

$$\alpha^{n+1}=\alpha^n+\Delta t\alpha',\quad \beta^{n+1}=\beta^n+\Delta t\beta' \tag{18}$$

where α' and β' are obtained from (9) and (10), considering $\theta(\beta^+,t)=1/2$, i.e.,

$$\beta'=-2h^2(\beta^n)\partial_x p^n(\beta^{n-}) \tag{19}$$

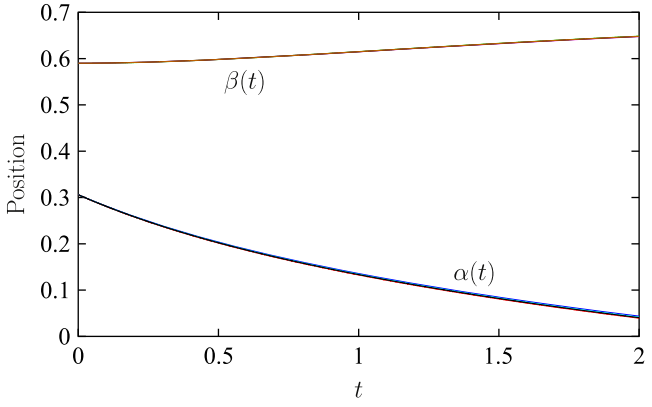

Fig. 7. $\alpha(t)$ and $\beta(t)$ for different grid resolutions for the first case with $(h\theta)(x_\ell,t)=0.65$.

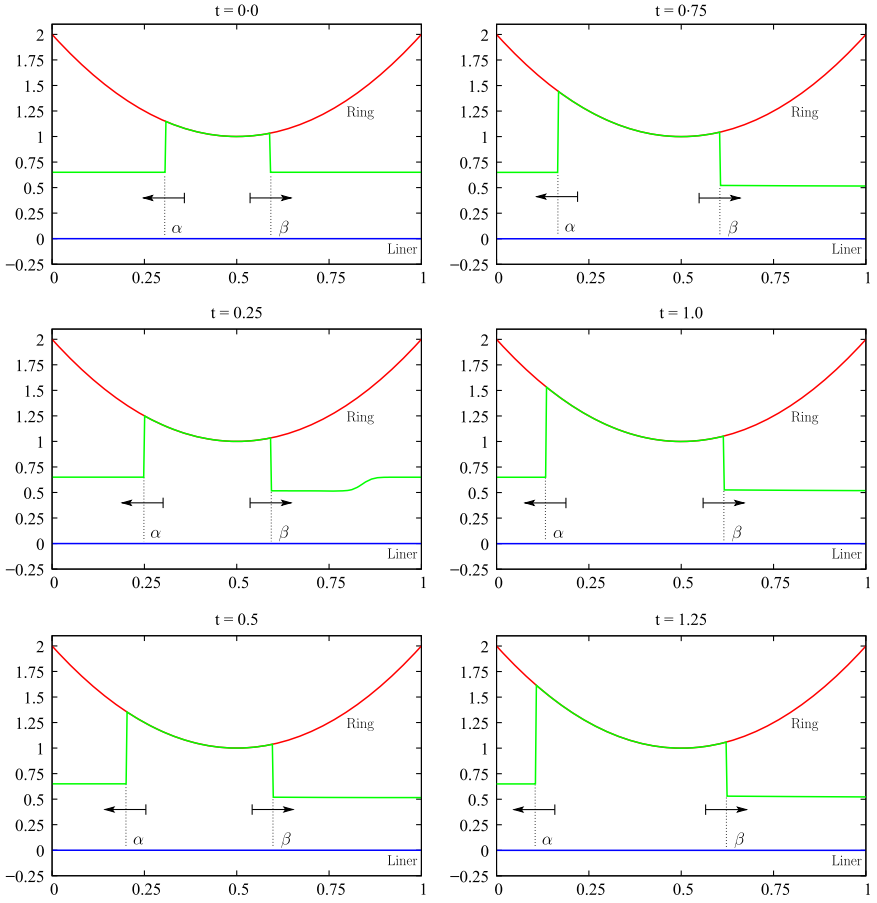

Fig. 6. Film profiles at different times for the single ring test for $(h\theta)(x_\ell,t)=0.65$.

This is correct if the resulting β' is positive (and $<S$, which is always the case in the considered examples).
Otherwise, remember that the first step may result in negative pressures to the left of β^n, implying that $\partial_x p^n(\beta^{n-}) > 0$ and β' given by (19) negative. In this case, β^{n+1} is chosen such that $\beta^{n+1} \neq \beta^n$ and with a value given by one of the two options that we aim to test:

- Option 1: Find β^{n+1} such that $p^n(\beta^{n+1}) = 0$ by linearly interpolating the nodal values of p^n.
- Option 2: Find β^{n+1} such that $\partial_x p^n(\beta^{n+1}) = 0$ by quadratically interpolating the nodal values of p^n.

The two options are illustrated in Fig. 5. Option 2, though more difficult to implement, seems a better choice, since, looking for the point of zero pressure derivative when $\beta' < 0$ is consistent with the observation made in Remark 2. Note also that this can be seen as performing only one fixed-point iteration for solving $p^{n+1}(\beta^{n+1}) = \partial_x p^{n+1}(\beta^{n+1}) = 0$. Then, the velocity of the front is recomputed as

$$\beta' = \frac{\beta^{n+1} - \beta^n}{\Delta t} \tag{20}$$

3. *Numerically solve the transport equation for* θ^{n+1}: Once the cavitations fronts are updated, we compute the new values of θ on C^{n+1} ensuring that *the amount of oil is conserved* from one step to the other. Mass conservation is obtained by using a finite volume solver. Notice that (11) is an evolution equation (in time) on a domain that is time-dependent. The finite volumes thus move according to α' and β' and the result is projected (conserving mass) onto the fixed nodal positions. Clearly, the finite volumes immediately next to the cavitation boundaries (in red, in Fig. 4) have to be dealt differently from the rest of the (standard) finite volumes (in pink). This is now explained for the particular situation illustrated in Fig. 4 corresponding to $\alpha' < 0$ and $\beta' < 0$ and where the cavitation boundaries cross the cell nodes from one step to the other.

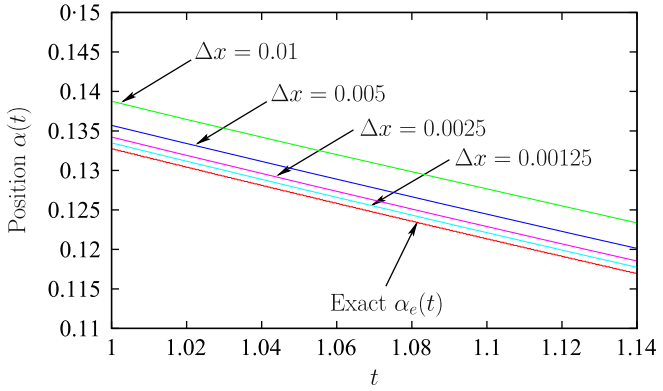

Fig. 8. Detail of $\alpha(t)$ for different grid resolutions for the first case with $(h\theta)(x_\ell, t) = 0.65$.

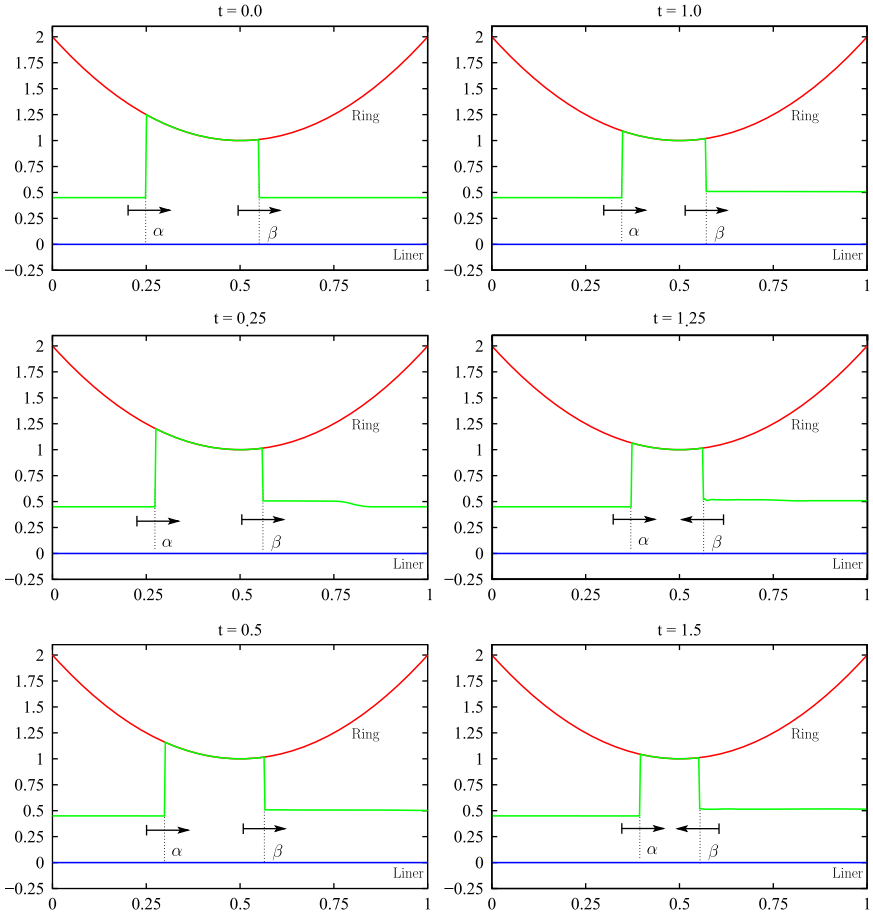

Fig. 9. Film profiles at different times for the single ring test with $(h\theta)(x_\ell, t) = 0.45$.

- For the standard finite volumes, we use a first-order (donor cell) scheme

$$h_i^{n+1}\theta_i^{n+1}\Delta x = h_i^n\theta_i^n\Delta x + S(h_{i-\frac{1}{2}}^n\theta_{i-1}^n - h_{i+\frac{1}{2}}^n\theta_i^n)\Delta t \quad (21)$$

where $h_{i\pm\frac{1}{2}}^n$ is the value of h^n evaluated at position $X_{i\pm\frac{1}{2}}$. If only discrete values are available for the distance field h, the cell faces values $h_{i-\frac{1}{2}}^n$ and $h_{i+\frac{1}{2}}^n$ can be computed as $(h_{i-1}^n + h_i^n)/2$ and $(h_i^n + h_{i+1}^n)/2$, respectively.

- For the finite volumes next to the cavitation boundaries we have: denoting by $i_\alpha \in C^{n+1}$ the first finite volume to the left of α^{n+1}, the value of $\theta_{i_\alpha}^{n+1}$ is computed from

$$h_{i_\alpha}^{n+1}\theta_{i_\alpha}^{n+1}(\alpha^{n+1} - X_{i_\alpha-\frac{1}{2}}) = h_{i_\alpha}^n\theta_{i_\alpha}^n(\alpha^n - X_{i_\alpha-\frac{1}{2}}) + h_{i_\alpha+1}^n\theta_{i_\alpha+1}^n \times(\alpha^n - \alpha^{n+1}) + [Sh_{i_\alpha-\frac{1}{2}}^n\theta_{i_\alpha-1}^n - (S-\alpha')h(\alpha^n)\theta_{i_\alpha}^n]\Delta t \quad (22)$$

Denoting by $i_\beta \in C^{n+1}$ the first finite volume to the right of β^{n+1}, the values of $\theta_{i_\beta}^{n+1}$ and $\theta_{i_\beta+1}^{n+1}$ are computed from

$$\theta_{i_\beta}^{n+1} = \theta(\beta^+, t^{n+1}) = \frac{\frac{S}{2} - \beta'(t)}{S - \beta'(t)} \quad (23)$$

$$h_{i_\beta+1}^{n+1}\theta_{i_\beta+1}^{n+1}\Delta x + h_{i_\beta}^{n+1}\theta_{i_\beta}^{n+1}(X_{i_\beta+\frac{1}{2}} - \beta^{n+1}) = h_{i_\beta+1}^n\theta_{i_\beta+1}^n(X_{i_\beta+\frac{3}{2}} - \beta^n) + [(S-\beta')h_{i_\beta+\frac{1}{2}}^n\theta_{i_\beta+1}^n - Sh_{i_\beta+\frac{3}{2}}^n\theta_{i_\beta+1}^n]\Delta t \quad (24)$$

We proceed in a similar way when the cavitation boundaries do not cross the cell nodes and/or the velocities α' and β' are positive.

4. Numerical experiments

4.1. Convergence test

We simulate a single parabolic ring moving with constant velocity $S=1$ and a smooth liner. The computational domain is the interval [0,1]. The distance between the two lubricated surfaces is given by

$$h(x) = 1 + (2x-1)^2 \quad (25)$$

We consider two different situations corresponding to the following initial conditions:

- $(h\theta)(x_\ell,t) = 0.65, \quad \alpha_0 = 0.30, \quad \beta_0 = 0.59$
- $(h\theta)(x_\ell,t) = 0.45, \quad \alpha_0 = 0.25, \quad \beta_0 = 0.55$

In these simple cases, the exact solution can be computed and then compared to the numerical predictions. First, in Fig. 6 we show the film profile at different times using a grid resolution $\Delta x = 0.0025$. For the first case, corresponding to $(h\theta)(x_\ell,t) = 0.65$, we show in Fig. 7 the position of the left and right fronts as a function of time using different grid resolutions, namely $\Delta x = 0.01, 0.005, 0.0025, 0.00125$. A time step Δt equal to 0.001 is used for the first mesh. The Courant number is kept constant for the rest of the simulations for which the time step is adjusted accordingly. A detail of Fig. 7 is shown in Fig. 8 to appreciate how the numerical solution converges to the exact one $\alpha_e(t)$ for the left (reformation) front. The convergence for the right (rupture) front $\beta(t)$ to $\beta_e(t)$ shows a similar behavior.

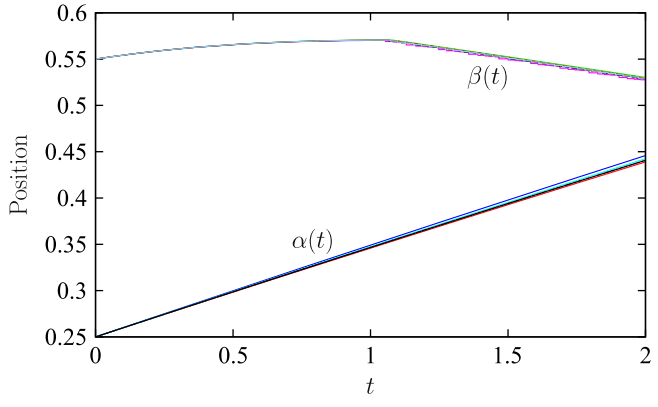

Fig. 10. $\alpha(t)$ and $\beta(t)$ for different grid resolutions for the second case with $(h\theta)(x_\ell,t) = 0.45$.

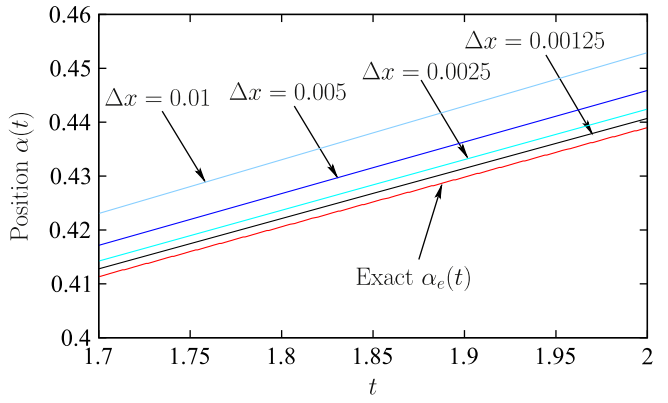

Fig. 11. Detail of $\alpha(t)$ for different grid resolutions for the second case with $(h\theta)(x_\ell,t) = 0.45$.

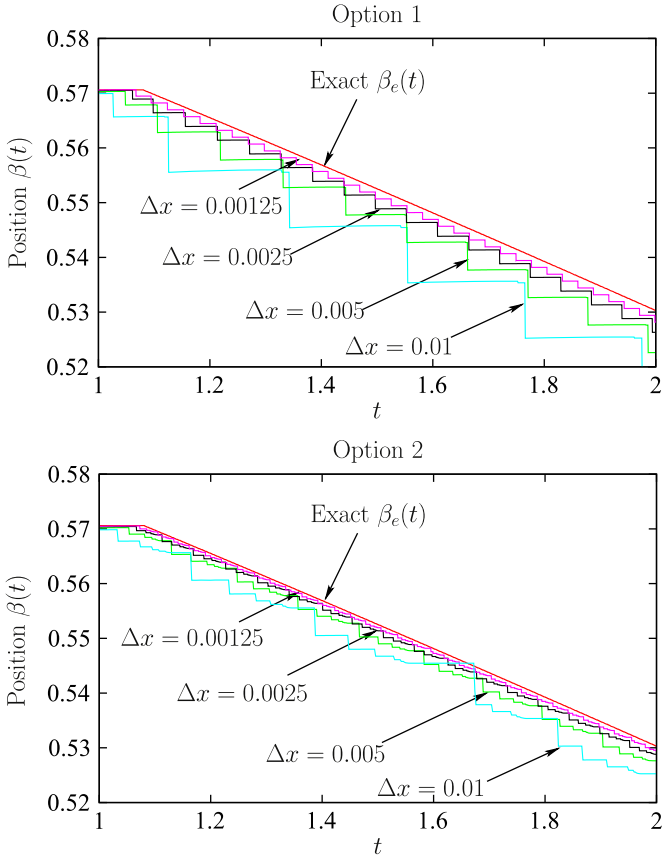

Fig. 12. Detail of $\beta(t)$ for different grid resolutions for the second case with $(h\theta)(x_\ell,t) = 0.45$ using the first option (top) and the second option (bottom) to treat the negative velocity of the rupture front.

For the second case, corresponding to $(h\theta)(x_\ell,t)=0.45$, in Fig. 9 we show the film profile at different times and in Fig. 10 we show the position of the left and right fronts as a function of time for the same grid resolutions used in the previous case. The reformation front moves to the right and the rupture front, initially moves to the right and at time $t\approx 1$, it starts moving to the left so as the pressurized region begins to reduce. The differences between the exact and numerical solutions are better seen in the details shown in Fig. 11 for the reformation front $\alpha(t)$ and in Fig. 12 for the rupture front $\beta(t)$ using the two options mentioned in Section 3. Notice the stair-case like behavior in both cases. This behavior is due to the type of algorithm chosen to deal with negative velocities of the rupture boundary. Results corresponding to the second option that involves the quadratic interpolation of the pressure nodal values are closer to the exact solution as seen in the figures.

Fig. 13 shows details at several instants of the film profiles using the two options for the second mesh considered. Qualitatively, the second option exhibits a better behavior. These differences become less evident as the mesh size and time step are refined. The corresponding convergence rates are shown in Fig. 14, where the maximum over t of $|\alpha(t)-\alpha_e(t)|$ (left) and $|\beta(t)-\beta_e(t)|$ (right) are plotted. By looking at the error of the β front (right part of Fig. 14), the convergence order is the same for both options, but, the error is smaller when the second one is used.

4.2. Textured-liner test

The aim in this case is to illustrate the differences between the new lubrication model and the Elrod–Adams model. The initial condition and geometry considered in this case is shown in Fig. 15. The computational domain is the interval $[-0.5,1]$. The total

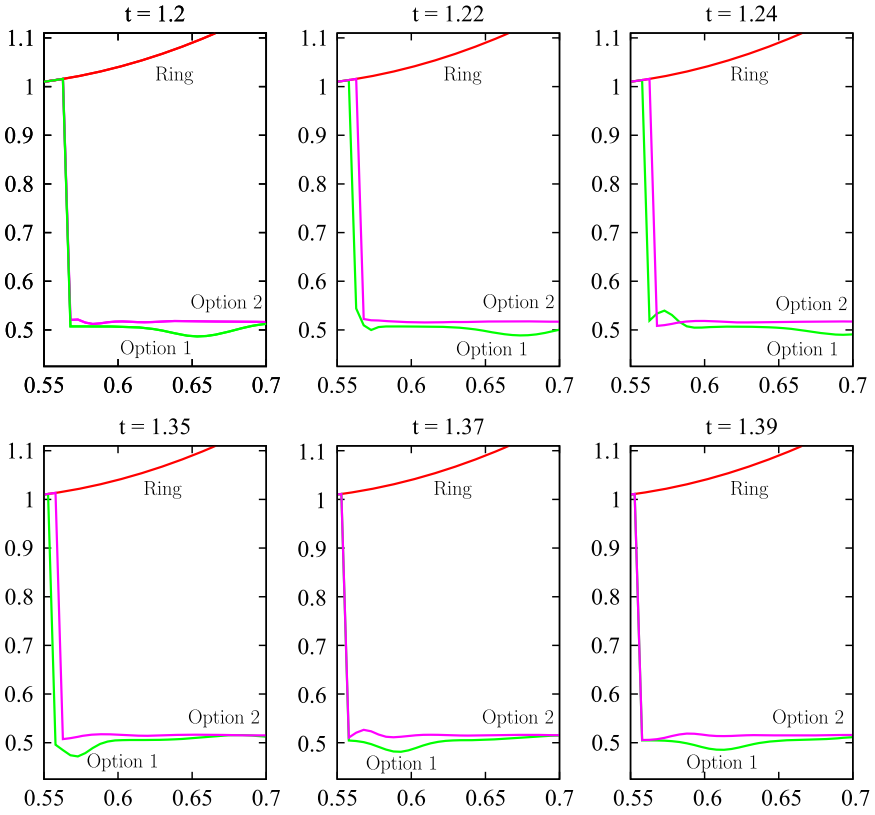

Fig. 13. Comparison of the film profiles at different instants using the two options to deal with the negative velocity of the rupture front in the case corresponding to $(h\theta)(x_\ell,t)=0.45$ for the second mesh with $\Delta x=0.005$.

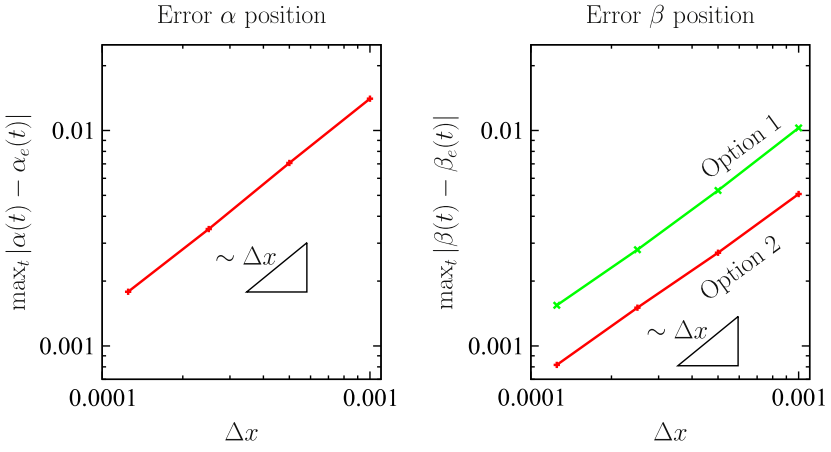

Fig. 14. Maximum error of $\alpha(t)$ (left) and $\beta(t)$ (right) as a function of Δx for the second case with $(h\theta)(x_\ell,t)=0.45$.

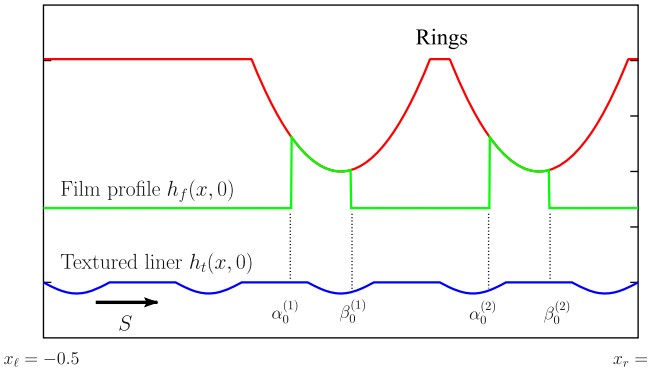

Fig. 15. Initial condition for the textured liner test showing the two rings and the moving texture.

distance between the two lubricated surfaces $h(x,t)$ has thus two contributions: one is the shape of the ring assembly $h_r(x)$ given by

$$h_r(x) = \begin{cases} 1+20\left(x-\frac{1}{4}\right)^2 & \text{if } 0.025 < x < 0.475 \\ 1+20\left(x-\frac{3}{4}\right)^2 & \text{if } 0.525 < x < 0.975 \\ 2 & \text{elsewhere} \end{cases} \tag{26}$$

and the other is the contribution of the moving texture on the liner, which is taken to be

$$h_t(x,t) = \max\{0, h_0 \sin[6(x-t)]\} \tag{27}$$

where h_0 is taken equal to 0.1. There are thus four fronts to be tracked in time whose initial positions are taken as

$$\alpha_0^{(1)} = 0.125, \quad \beta_0^{(1)} = 0.275 \tag{28}$$

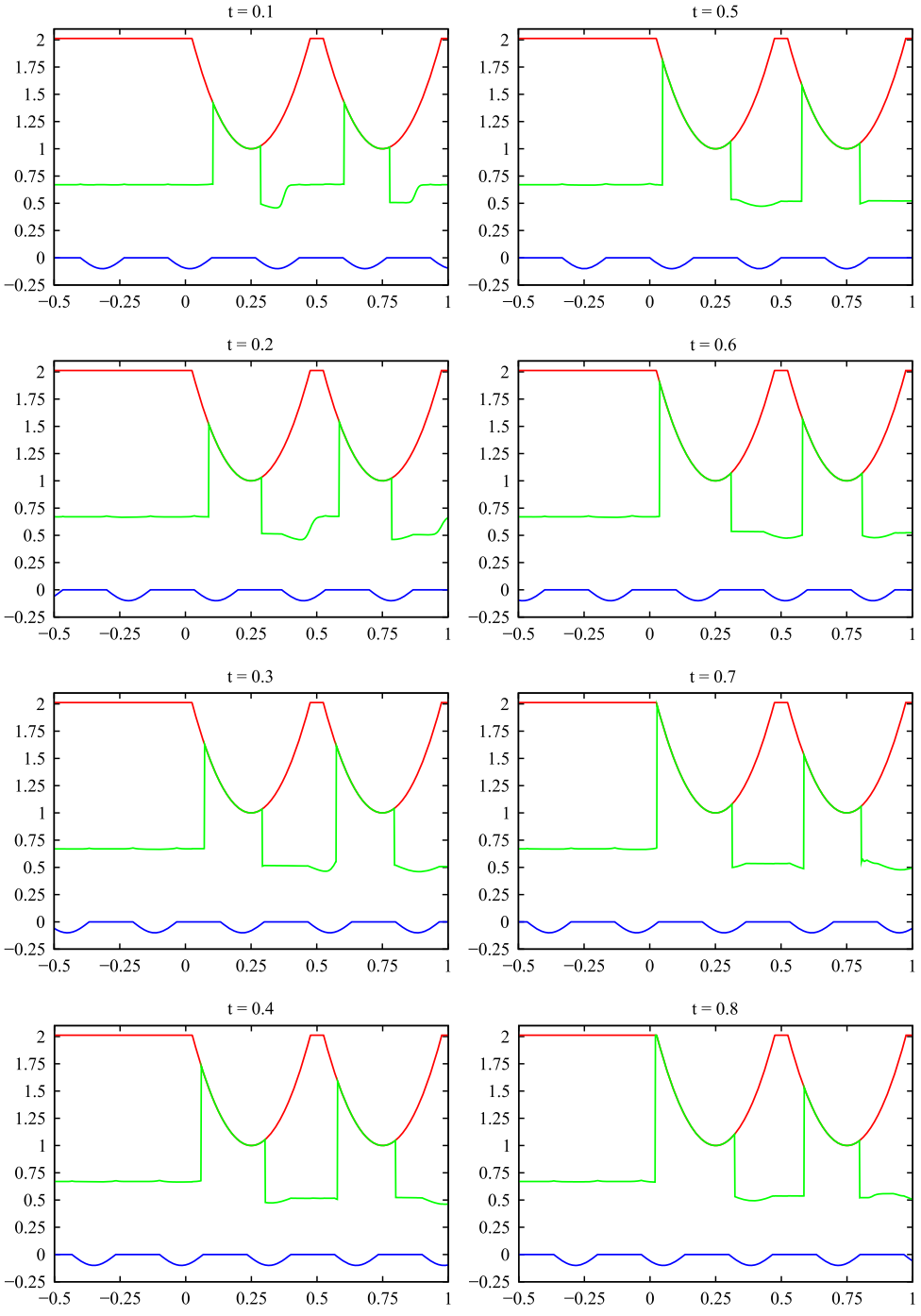

Fig. 16. Film profiles at different times for the textured-liner test using the new model.

$$\alpha_0^{(2)} = 0.625, \quad \beta_0^{(2)} = 0.775 \tag{29}$$

The mesh size Δx is set to 0.0015 and the time step Δt to 0.0001. The inlet film $h_f(x_\ell,t)$ is set to a fixed value of 0.67. To satisfy this boundary condition we adjust at each time step the value of $\theta(x=x_\ell,t)$ since $h(x=x_\ell,t)$ is not constant due to the moving texture. In Fig. 16 we show the film profile at different times.

We also simulate the same problem with the Elrod–Adams $p-\theta$ model. As mentioned before, this problem is important because the behavior of the second ring can be very much affected by the first (upstream) ring. In this case, in order to perform a fairer comparison, we consider an inlet film height $h_f(x_\ell,t)$ equal to 2×0.67, that corresponds in this model to the same inlet flow used for the simulations using the new model. Results are shown in Fig. 17. There are remarkable differences between the two models. First, since according to the Elrod–Adams model the texture travels at velocity $S=1$ while the saturation field θ is transported with velocity $S/2$ in the cavitated region, the film profile results perturbed in the left region $(-0.5,\alpha^{(1)}(t))$, while for the new model the film profile remains flat. Second, the fronts move with different velocities in each model, leading to a different temporal evolution of the pressurized region for each ring. We illustrate this difference in Fig. 18 where the pressure profiles for both models at selected times are plotted. Third, the new model predicts a discontinuity at the

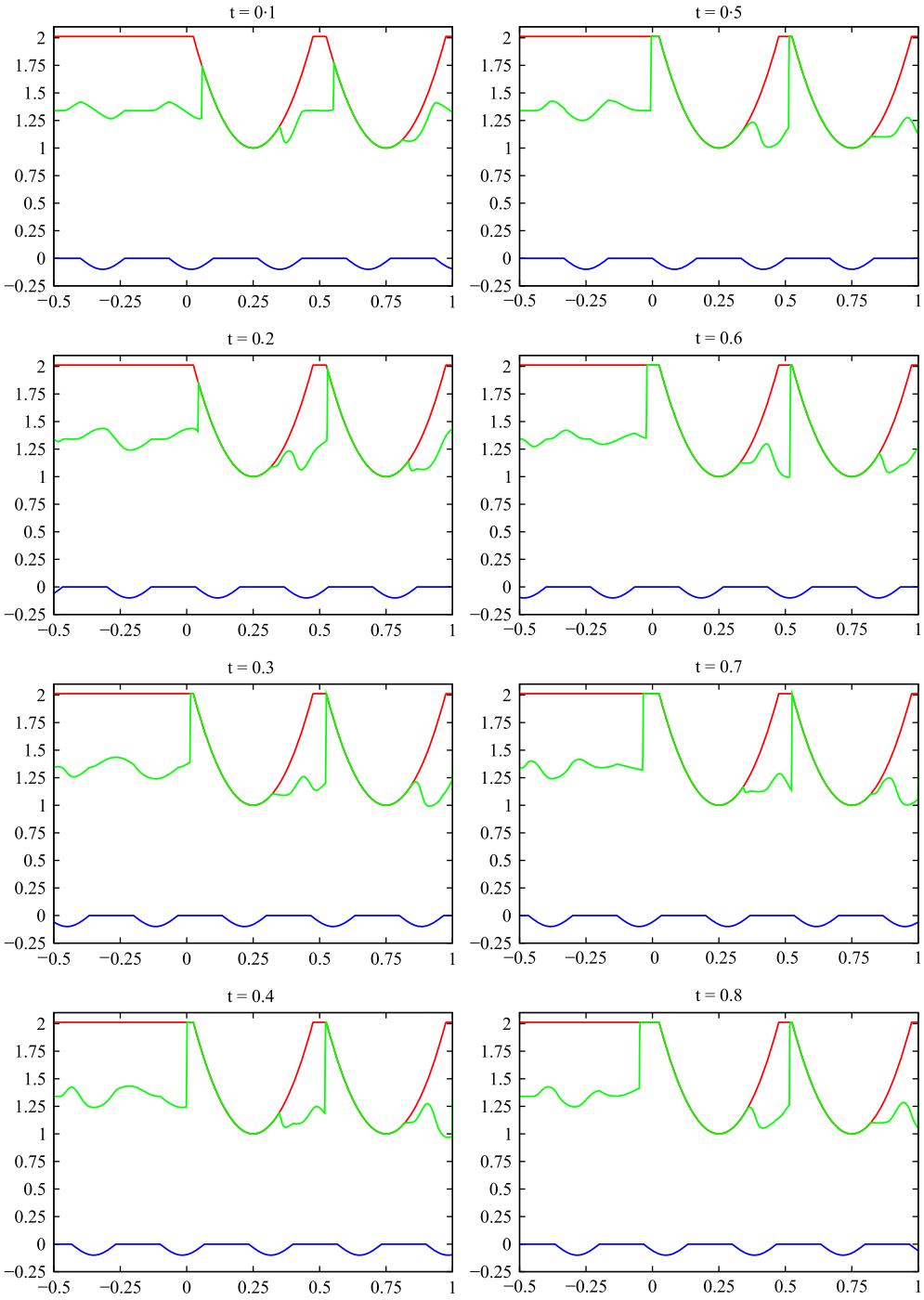

Fig. 17. Film profiles at different times for the textured-liner test using the Elrod–Adams $p-\theta$ model.

rupture boundaries $\beta^{(1)}$ and $\beta^{(2)}$ which does not occur with the Elrod–Adams model.

4.3. Dynamical test

In this final numerical test we consider again just one single ring in the domain [0,1], and solve the dynamical equilibrium equation for the ring simultaneously with the governing equations using the new model. We consider the ring shape given by

$$h(x,t) = h_m(t) + (2x-1)^2 \tag{30}$$

Denoting by $W^a(t)$ the applied load and by M the mass of the piston ring, the dynamical equilibrium equation can be written for the minimum film thickness $h_m(t)$ as

$$M\frac{d^2h_m(t)}{dt^2} = W(t) + W^a(t) \tag{31}$$

where the load carrying capacity is given by

$$W(t) = \int_{x_\ell}^{x_r} p(x,t)\,dx = \int_{\alpha(t)}^{\beta(t)} p(x,t)\,dx \tag{32}$$

since the pressure is zero in the cavitated region. The numerical procedure to solve the problem is based on a Newmark scheme as done in [20,13], in which we compute the new position and velocity according to

$$h_m^{n+1} = h_m^n + \Delta t V^n + \frac{\Delta t^2}{2M}[W^a(t^n) + W^n] \tag{33}$$

$$V^{n+1} = V^n + \frac{\Delta t}{M}[W^a(t^n) + W^n] \tag{34}$$

where V^n is an approximation for $\dot{h}_m(t^n)$.

For the simulation we use a mesh size $\Delta x = 0.004$, a time step $\Delta t = 0.0004$ and consider a piston ring mass M equal to 10^{-6} and an inlet film h_f=0.65. The problem is solved for two different applied loads:

- Constant load: $W^a = -0.004$
- Time dependent load: $W^a(t) = -0.0004 + 0.00005\cos(2\pi t)$

The second option corresponding to the quadratic interpolation of the pressure was used to deal with the case of negative velocities at rupture points. First, we show the evolution of $h_m(t)$ for both cases in Fig. 19. In the first case, the position of the ring assumes a steady state value while for the second case, a periodic behavior of $h_m(t)$ is observed. This behavior is also observed if we plot the position of the cavitation fronts $\alpha(t)$ and $\beta(t)$ for both types of applied loads. This is shown in Fig. 20. This example already shows that the proposed algorithm is capable of dealing with a more complicated transient situation.

5. Conclusions

The main objective of this paper has been the presentation of a finite volume implementation of the new lubrication model recently introduced in [27], which can be seen as a variant of the Elrod–Adams model but deals in a more realistic way with the peculiarities of piston–ring/liner systems. The proposed algorithm

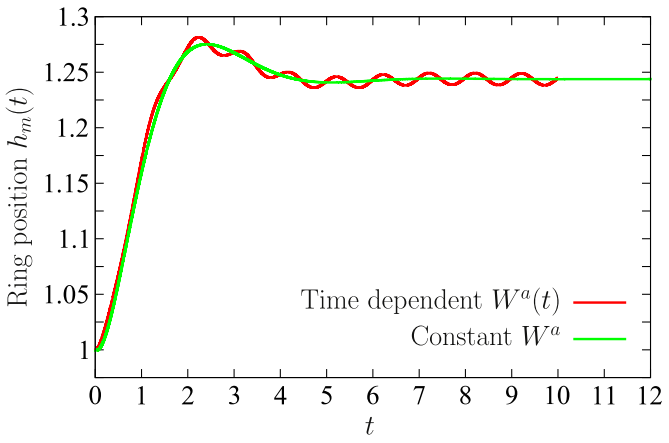

Fig. 19. Resulting ring position $h_m(t)$ in the dynamical test problem for the case with a constant applied load (green) and the case with a time dependent applied load (red). (For interpretation of the references to color in this figure caption, the reader is referred to the web version of this article.)

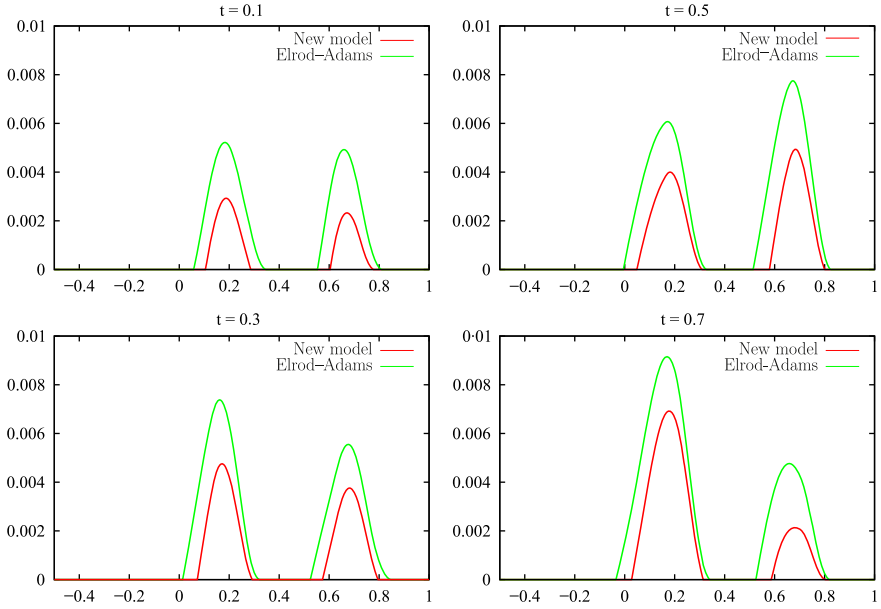

Fig. 18. Comparison of non-dimensional pressure profiles at different times using the new model (red) and the Elrod–Adams $p-\theta$ model (green). (For interpretation of the references to color in this figure caption, the reader is referred to the web version of this article.)

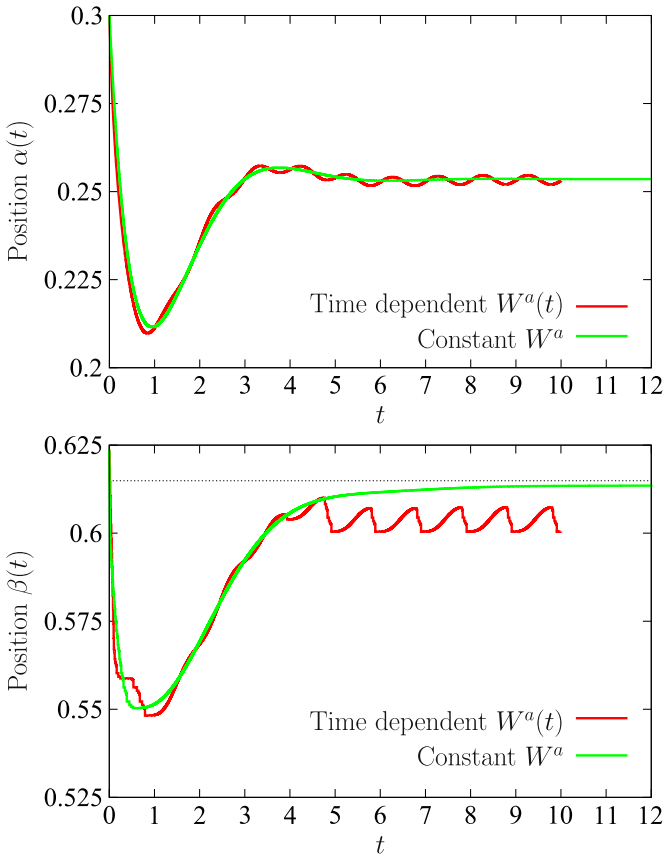

Fig. 20. Resulting $\alpha(t)$ and $\beta(t)$ in the dynamical test problem for the case with a constant applied load (green) and the case with a time dependent applied load (red). (For interpretation of the references to color in this figure caption, the reader is referred to the web version of this article.)

for this new model is based on a finite volume scheme with an explicit tracking of the cavitation fronts so as to impose the appropriate boundary condition for the saturation field depending on the velocities of such fronts. Although in this paper we have focused on the one-dimensional case with constant sliding velocity, the need for a new model and the numerical challenges involved are already observed. Three different tests have been presented. The first one, consisting in the simulation of a single ring of parabolic shape with a smooth liner, a problem for which an exact solution can be found, aimed to show that the proposed numerical procedure gives convergent solutions. The second test, that dealt with a more complicated setting, included two rings of parabolic shape and a moving texture of sinusoidal shape. In this case, a comparison to the Elrod–Adams model has been done to show the fundamental differences between the two models. Finally, in the third example, the dynamical behavior of one ring was modeled by means of additionally solving the equation of motion of the ring to show that the numerical algorithm is capable of dealing with more severe transient situations.

The extension of the present numerical scheme to two dimensions and to the case of a time dependent sliding velocity (of alternating sign) is not immediate, since new ingredients appear that need proper numerical treatment. In particular, the boundary value at Σ for the transport of θ depends on whether it is a reformation boundary or a rupture boundary. The cells at the boundary of the cavitated region, in the Elrod–Adams formulation, take their boundary values from the pressurized region, where $\theta=1$. This makes the algorithm very simple. For the new model, the boundary value can no longer come from the neighboring pressurized cell (where $\theta=1$ as before) when in rupture, but instead be given by $G(\beta')$ (Eq. (15)). This will complicate the two-dimensional version of the algorithm, both by having to discern rupture boundaries from reformation boundaries and by having to compute a suitable approximation to the front speed at each rupture cell. At reformation boundaries, on the other hand, the code will be essentially equivalent to an Elrod–Adams one. A suitable implementation is the subject of ongoing work.

Acknowledgments

The authors acknowledge partial support from FAPESP (Brazil), CNPq (Brazil) and Renault (France). This research was carried out in the framework of INCT-MACC, Ministério de Ciência e Tecnologia, Brazil.

References

[1] Priest M. The wear and lubrication of piston rings. PhD thesis. University of Leeds; 1996.
[2] Priest M, Dowson CM, Taylor D. Predictive wear modelling of lubricated piston rings in a diesel engine. Wear 1999;231(1):89–101.
[3] Priest M. Factors influencing boundary friction and wear of piston rings. Tribology Series 2000;38:409–16.
[4] Ma M-T, Smith E, Sherrington I. A three-dimensional analysis of piston ring lubrication. Part 1: modelling. Proceedings of the Institution of Mechanical Engineers 1995;209(1):1–14.
[5] Ma M-T, Smith E, Sherrington I. A three-dimensional analysis of piston ring lubrication. Part 2: sensitivity analysis. Proceedings of the Institution of Mechanical Engineers 1995;209(1):15–27.
[6] Uehara Y, Wakuda M, Yamauchi Y, Kanzaki S, Sakaguchi S. Tribological properties of dimpled silicon nitride under oil lubrication. Journal of the European Ceramic Society 2004;24:369–73.
[7] Wakuda M, Yamauchi Y, Kanzaki S, Ysuda Y. Effect of surface texturing on friction reduction between ceramic and steel materials under lubricated sliding contact. Wear 2003;254:356–63.
[8] Yagi K, Takedomi W, Tanaka H, Sugimura J. Improvement of lubrication performance by micro pit surfaces. Tribology Online 2008;3:285–8.
[9] Yu H, Wang X, Zhou F. Geometric shape effects of surface texture on the generation of hydrodynamic pressure between conformal contacting surfaces. Tribology Letters 2010;37:123–30.
[10] Zum Gahr K, Mathieu M, Brylka B. Friction control by surface engineering of ceramic sliding pairs in water. Wear 2007;263:920–9.
[11] Organisciak M, Cavallaro G, Lubrecht A. Starved hydrodynamic lubrication of the piston ring cylinder liner contact: preliminary study of the influence of surface texturing. Tribology and Interface Engineering Series 2005;48:573–83.
[12] Organisciak M, Cavallaro A, Lubrecht G. Influence of the cross-hatched surface texture on a starved hydrodynamic linear contact. ASME conference proceedings (IJTC2007-44144); 2007. pp. 905–7.
[13] Buscaglia G, Jai M, Cadalenc J-P, Choukrounc F. Mass-conserving numerical simulation of piston ring/liner contact along a full engine cycle. Mecánica Computacional 2010;XXIX:3257–79.
[14] Elrod HG, Adams M. A computer program for cavitation. Technical report 190. First LEEDS LYON symposium on cavitation and related phenomena in lubrication, I.M.E.; 1974, 103:354.
[15] Jakobson B, Floberg L. The finite journal bearing considering vaporization. Transactions on Chalmers University of Technology 1957:354.
[16] Olsson K. Cavitation in dynamically loaded bearings. Transactions on Chalmers University of Technology 1965;308.
[17] Kumar A, Booker J. A finite element cavitation algorithm. ASME Journal of Tribology 1991;113:276–86.
[18] Boedo S, Booker J. Cavitation in normal separation of square and circular plates. ASME Journal of Tribology 1995;117:403–10.
[19] Optasanu V, Bonneau D. Finite element mass-conserving cavitation algorithm in pure squeeze motion. Validation/application to a connecting rod small end bearing. Transactions of the ASME 2000;122:162–9.
[20] Ausas R, Jai M, Buscaglia G. A mass-conserving algorithm for dynamical lubrication problems with cavitation. ASME Journal of Tribology 2009;132:031702 (7 pages).
[21] Ausas R, Ragot P, Leiva J, Jai M, Bayada G, Buscaglia G. The impact of the cavitation model in the analysis of micro-textured lubricated journal bearings. ASME Journal of Tribology 2007;129:868.
[22] Etsion I, Pinkus O. Analysis of short journal bearings with new upstream boundary conditions. Journal of Lubrication Technology, Transactions on ASME 1974;96:489–96.

[23] Dowson D, Taylor C. Cavitation in bearings. Annual Review of Fluid Mechanics 1979;11:35–65.
[24] Ausas R. Numerical simulation of two-phase immiscible flows with applications to hydrodynamic lubrication. PhD thesis. Engineering, Instituto Balseiro; April 2010.
[25] Buscaglia GC, Ausas RF. Variational formulations for surface tension, capillarity and wetting. Computer Methods in Applied Mechanics and Engineering 2011;200(45–46):3011–25.
[26] Organisciak M. Optimisation de la microgeometrie des chemises de moteurs a combustion interne. PhD thesis. l'Institut National des Sciences Appliquées de Lyon; 2007.
[27] Buscaglia G, Ciuperca I, Jai M. A new cavitation model in lubrication. Journal of Engineering Mathematics, submitted for publication.